Neutron Diffraction Study of a Sintered Iron Electrode In Operando

Weninger, B.; Thijs, M.A.; Nijman, Jeroen A.C.; van Eijck, L.; Mulder, F.M.

Important note
To cite this publication, please use the final published version (if applicable).
Please check the document version above.

Article

Neutron Diffraction Study of a Sintered Iron Electrode In Operando

Bernhard M. H. Weninger, Michel A. Thijs, Jeroen A. C. Nijman, Lambert van Eijck, and Fokko M. Mulder*

Read Online

ACCESS | Metrics & More | Article Recommendations | Supporting Information

ABSTRACT: Iron is a promising, earth-abundant material for future energy applications. In this study, we use a neutron diffractometer to investigate the properties of an iron electrode in an alkaline environment. As neutrons penetrate deeply into materials, neutron scattering gives us a unique insight into what is happening inside the electrode. We made our measurements while the electrode was charging or discharging. Our key questions are: Which phases occur for the first and second discharge plateaus? And why are iron electrodes less responsive at higher discharge rates? We conclude that metallic iron and iron hydroxide form the redox pair for the first discharge plateau. For the second discharge plateau, we found a phase similar to feroxyhyte but with symmetrical and equally spaced arrangement of hydrogen atoms.

The data suggest that no other iron oxide or iron (oxy)hydroxide formed. Remarkable findings include the following: (1) substantial amounts of iron hydroxide are always present inside the electrode. (2) Passivation is mostly caused by iron hydroxide that is unable to recharge. (3) Iron fractions change as expected, while iron hydroxide fractions are delayed, resulting in substantial amounts of amorphous, undetectable iron phases. About 40% of the participating iron of the first plateau and about 55% of the participating iron for the second plateau are undetectable. (4) Massive and unexpected precipitation of iron hydroxide occurs in the transition from discharging to charging. (2), (3), and (4) together cause accumulation of iron hydroxide inside the electrode.
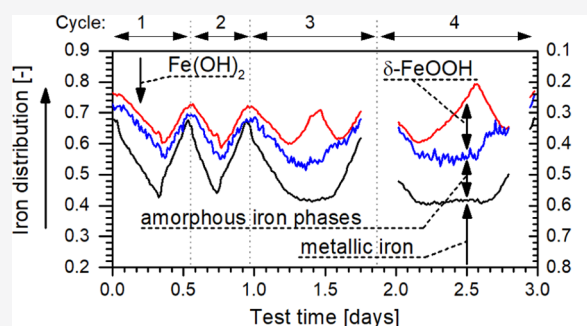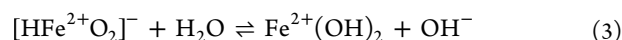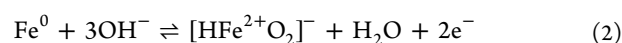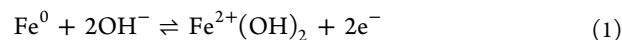
INTRODUCTION

The development and implementation of renewable electricity generation increasingly ask for electrochemical energy storage and conversion based on earth-abundant materials. Iron is a low-cost and earth-abundant material, which can be used for energy storage and conversion. Here, we use a neutron diffractometer to study an iron electrode in operando.

As an energy storage material, iron works as a negative electrode. At high pH, metallic iron and iron hydroxide can be in a reversible phase equilibrium at a potential that is slightly more negative than the potential of the reversible hydrogen electrode. The nickel−iron battery as invented by Jungner and Edison combines iron anodes with nickel cathodes. When such batteries are overcharged, they electrolyze the water in the electrolyte to form hydrogen and oxygen. In a battolyser,[1,2] the hydrogen is collected, combining the storage and conversion function in one device. Replacing the positive nickel electrode with a reversible oxygen electrode creates the iron−air battery. Recently, there has been a renewed interest in iron−air batteries as they promise high energy density combined with a reduced nickel content.[3−6] Iron electrodes have recently been proposed as means to decouple oxygen and hydrogen generation.[7−10] To do so, the iron electrode is located in between the cathode and the anode to delay hydrogen generation. The resulting system can release its stored energy

electrically or as hydrogen. This versatility makes iron electrodes promising for future energy applications.

Iron electrodes have two discharge plateaus. The first plateau is the two-electron transition from Fe^0 to Fe^{2+}. The second plateau is the one-electron transition from Fe^{2+} to Fe^{3+}. Battery operation is usually restricted to the first plateau due to the limited reversibility of the second plateau. The first plateau is a dissolution−precipitation reaction. The dissolution process is strongly dependent on pH, potential, and temperature.[11,12] Reaction (1) (−0.88 V relative to standard hydrogen electrode, SHE) provides the overall reaction scheme for the first plateau. Reaction 1 is composed of the reaction steps for dissolution (2) and precipitation (3)
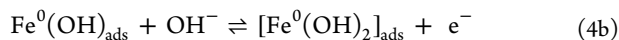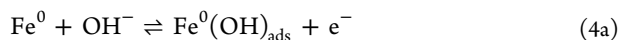
$$Fe^0 + 2OH^- \rightleftharpoons Fe^{2+}(OH)_2 + 2e^- \quad (1)$$

$$Fe^0 + 3OH^- \rightleftharpoons [HFe^{2+}O_2]^- + H_2O + 2e^- \quad (2)$$

$$[HFe^{2+}O_2]^- + H_2O \rightleftharpoons Fe^{2+}(OH)_2 + OH^- \quad (3)$$

The dissolution process (2) can be further split into[13]

$$Fe^0 + OH^- \rightleftharpoons Fe^0(OH)_{ads} + e^- \qquad (4a)$$

$$Fe^0(OH)_{ads} + OH^- \rightleftharpoons [Fe^0(OH)_2]_{ads} + e^- \qquad (4b)$$

$$[Fe^0(OH)_2]_{ads} + OH^- \rightleftharpoons [HFe^{2+}O_2]^- + H_2O \qquad (4c)$$

Note that reactions 3 and 4c are not electrochemical reactions but regular chemical reactions with pH- and temperature-dependent equilibria.

Some of these iron species are soluble. For Fe^{2+}, this is $HFeO_2^-$ (hydrated as $Fe(OH)_3^-$). Soluble Fe^{3+} is FeO_2^- (hydrated as $Fe(OH)_4^-$). Fe^{2+} and Fe^{3+} are in equilibrium in highly alkaline solutions. During battery operation, the dissolution from Fe to Fe^{2+} is likely the rate-limiting step for discharging. Equilibration between soluble Fe^{2+} and Fe^{3+} species appears to be fast.[14]

Recent work[15] suggests an oxidation path from iron to magnetite (Fe_3O_4) via a soluble intermediate. In this case, reaction 3 would be replaced by reaction 5. The net overall reaction then becomes reaction (6) (-0.91 V vs SHE)

$$3HFeO_2^- + H^+ \rightarrow Fe_3O_4 + 2H_2O + 2e^- \qquad (5)$$

$$3Fe + 8OH^- \rightarrow Fe_3O_4 + 4H_2O + 8e^- \qquad (6)$$
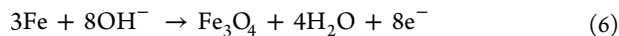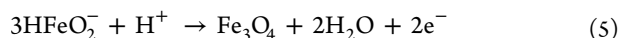
Such a more direct oxidation from iron to magnetite, without the intermediate iron hydroxide, is also observed for systems with nanosized iron particles.[16] Thermodynamically, both reactions are possible. The equilibrium potential for the reactions from iron to iron hydroxide and from iron to magnetite is close to each other.[17] Dehydrated iron compounds are slightly more stable than hydrated compounds. Iron hydroxide can be oxidized to magnetite according to the Schikorr reaction 7. This reaction is slow at room temperature but faster at higher temperatures[18]

$$3Fe(OH)_2 \rightarrow Fe_3O_4 + 2H_2O + H_2 \qquad (7)$$
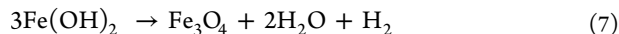
Metallic iron is not stable under highly alkaline conditions. The corrosion process produces hydrogen through reaction 8

$$Fe + 2H_2O \rightarrow Fe(OH)_2 + H_2 \qquad (8)$$
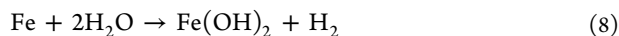
Iron hydroxide can be oxidized to any iron oxide or (oxy)hydroxide, except γ-FeOOH. All other iron oxide/(oxy)hydroxides should be evaluated as possible reaction products of the second discharge plateau. The structure of $Fe(OH)_2$ is stable until the Fe^{3+} content reaches 10% of the total iron content. In strongly alkaline solutions, like our electrolyte, $Fe(OH)_2$ is oxidized to $Fe(OH)_3$ first and then dehydrated to FeOOH.[19] The second discharge reaction can be written as reaction (9) (-0.56 V relative to SHE),[20] considering iron hydroxide and iron oxyhydroxide

$$Fe^{2+}(OH)_2 + OH^- \rightleftharpoons Fe^{3+}OOH + H_2O + e^- \qquad (9)$$
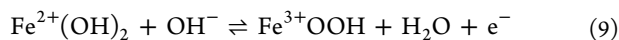
δ-FeOOH and/or Fe_3O_4 are the discharge products most commonly identified for the second discharge plateau. Higher temperatures and continuous cycling favor the formation of Fe_3O_4. Moreover, Fe_3O_4 is always found when the electrolyte contains LiOH, a common electrolyte additive.[21−23] In situ Mössbauer spectroscopy supports this finding, Fe_3O_4 is the discharge product of the second discharge plateau in an electrolyte-containing lithium hydroxide, whereas pure KOH electrolyte leads to the formation of β-FeOOH.[24] A recent in situ X-ray diffraction (XRD) study links the presence of δ-

FeOOH to the oxidation of iron hydroxide but points out that δ-FeOOH is only an intermediate toward the formation of Fe_3O_4 upon dehydration, and Fe_3O_4 is identified as the main product of the second discharge step.[15] Here, electrodes were prepared with and without the BiS_2 additive. Interestingly, iron hydroxide and δ-FeOOH were only detected with samples containing BiS_2. Otherwise, only Fe_3O_4 was detected as the crystalline phase for the first and second discharge plateaus. According to the authors, iron hydroxide may be present, but undetectable, in an amorphous phase. Additionally, γ-Fe_2O_3 was recently identified by Raman spectroscopy as the discharge product of the second discharge stage where it forms large crystals.[25] Note that γ-Fe_2O_3 (maghemite) and Fe_3O_4 (magnetite) are isostructural and can hardly be distinguished in XRD patterns.

The operating conditions (e.g., charge/discharge rates) and/or additives determine which discharge products are formed.[15,22] To exclude these effects, we study the iron−water system without any additives to either electrode or electrolyte. Our electrolyte was a 25% KOH solution by weight, and our electrodes were made of pure, sintered iron. In this study, we conducted neutron diffraction measurements while the electrode was charging, overcharging (electrolyzing), or discharging. This allowed us to observe the different crystallographic phases that are present. Hydrogen causes incoherent neutron scattering increasing the background signal level. This allows us to see the hydrogen and electrolyte contents inside the sample. As neutrons penetrate deeply into materials, neutron scattering gives us a unique insight into what is occurring inside of the electrode, rather than on the surface.

■ EXPERIMENTAL SECTION

Electrode Production. In this study, sintered iron electrodes are investigated. The production is based on the process as described by Falk and Salkind.[26] This is the classical route for the production of iron oxides for pocket electrodes. The synthesis starts with iron(II) sulfate heptahydrate (VWR Chemicals, ≥98%, GPR Rectapur). First, the iron sulfate was dried to monohydrate at 100 °C. Then, the powder was oxidized to hematite (Fe_2O_3) at 800 °C. Energy-dispersive X-ray spectroscopy (EDX) was used to confirm that no sulfur remained after oxidation. Reduction took place in a flow-through reactor at 550 °C with hydrogen as the reducing agent. This temperature avoids sintering of the reduced iron powder during this stage of synthesis. The sintering threshold temperature, or Tammann temperature, of a solid is roughly half the melting temperature in K. For iron, this is 906 K (633 °C).[27] The reactor was left to cool to room temperature in a reducing Ar/H_2 atmosphere. After cooling, the reactor was moved into an argon-filled glovebox. The reduced iron was carefully ground inside a glovebox. The resulting powder was pressed into tube shapes at a pressure of 300 kg/cm^2. These tube sections were sintered at 750 °C under an Ar/H_2 atmosphere. Reduced iron powders and iron electrodes remained inside the argon-filled glovebox where possible to limit oxidation. The active electrode material was only exposed to air during pressing and cell assembly. Exposure to air causes the formation of a passivation layer on the surface of the electrode. This passivation layer was removed electrochemically.

In total, 12 electrode sections were produced with the following dimensions: total weight: 6.58 g Fe, average porosity:

64.3%, average inner diameter: 3.23 mm, average outer diameter: 7.53 mm, and total height: 64.5 mm. These dimensions were chosen to maximize the iron content inside the sample holder for neutron diffraction experiments. A porosity of 64.3% should provide a stable iron electrode with a reasonable material utilization. Higher porosities may yield a higher material utilization, but a higher conversion may cause disintegration of the sintered iron body together with a loss of essential electrical conductivity.[6] Figure S1 of the Supporting Information (SI) provides additional characterization for the iron powder.

Electrodes produced in this way work right away as they consist of porous iron. Initial charging of about 15 min is sufficient to remove the passivation layer from the surface. The electrode can then be discharged.

Cell Assembly. To assemble the cell, the 12-tube sections were mounted in a quartz tube sample holder. The nickel-wire counter electrode, necessary for cell operations during the diffraction measurements, was placed in the center of the tube sections.

In the headspace above the iron electrode, an Hg/HgO reference electrode was inserted. This electrode provided the voltage reference for the measurement of the iron electrode potential. The headspace remained outside of the neutron beam. Figure 1 shows the used setup during preliminary testing. The inset shows one of the tube sections after pressing. Figure S2 shows additional pictures of the setup that was used.

Initial considerations led to the conclusion that water (H_2O) should be used for the tests rather than heavy water (D_2O). Deuterium hardly causes any incoherent scattering. This would reduce the background intensity. Normally, hydrogen does cause a substantial background. This allowed us to investigate the hydrogen-related densities inside the system by analyzing variations of the background signal during operations. Previous experience in hydrogen storage materials also indicates that protonated samples still give good signal-to-noise ratios in modern diffractometers.[28] The use of H_2O left us enough diffraction signal intensity above background to be able to identify the phases quantitatively.

When a cell is discharged to the first discharge plateau for the first time, it shows a higher capacity than on subsequent discharges. In this study, we found about 0.40 Ah/g_{Fe} for the first discharge. Subsequent cycles yield lower capacities of about 0.15 Ah/g. To condition the electrode before measurement, it was cycled eight times and then fully charged. Prior to measurement, the electrode was set on an additional floating charge (30 mA) for 24 h.

The sintered iron electrode we produced was discharged to a capacity of 0.21 Ah/g_{Fe} to study the first discharge plateau. To study the second discharge plateau, it was discharged to a capacity of 0.42 Ah/g_{Fe}. Geometric factors play an important role in determining material utilization. Thinner electrodes have advantages and show a higher utilization (see e.g., ref 6). For a proper comparison of geometric factors like thickness, counter electrode position, and current density, information about the electrode and electrolyte additives needs to be reported and considered.[5] Here, we produced a pure iron electrode with a tubular shape and a wall thickness of 2.15 mm, with neither electrode additives nor electrolyte additives, and a Ni-wire counter electrode in the center. The volumetric energy density for the first discharge plateau results in 0.59 Ah/cm^3 excluding the space for the counter electrode and to 0.48 Ah/cm^3 including that space.
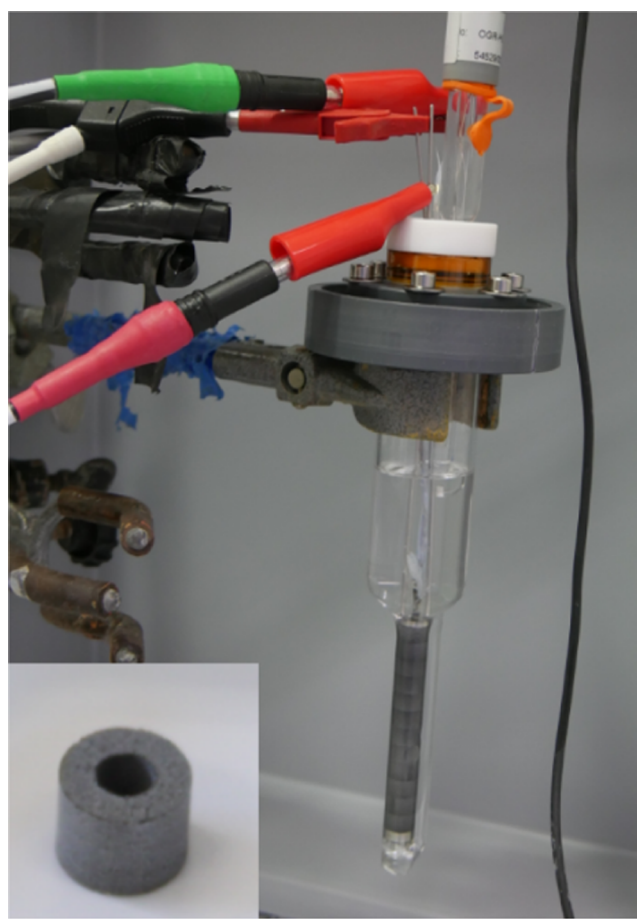

Figure 1. Preliminary testing of the electrode. The setup comprises the tubular iron electrode, the centered nickel counter electrode, and a Hg/HgO reference electrode, which senses the headspace. A capillary in the back connects the headspace with the bottom of the cell to provide the electrolyte. Inset: one tube section after pressing.
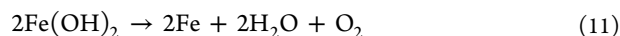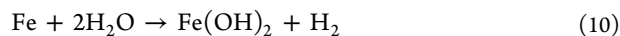
In Operando Neutron Diffraction. In operando neutron diffraction data was collected with the Pearl instrument at the Reactor Institute Delft.[29] This instrument uses thermal neutrons. A monochromator allows the selection of four different wavelengths of neutrons. For this study, we used a wavelength of 1.667 Å. The setup has a fixed multipixel detector with a $2\Theta_M$ range of 150° over 1408 pixels. The recording time of each neutron diffraction pattern was set to 15 min. Two hundred and forty-seven diffractograms were collected in three sessions: (1) patterns 0−167, (2) patterns 192−266, and (3) patterns 281−284.

This study contains four electrochemical cycles of discharging and then recharging. In the first two cycles, we investigate the phase changes for the first iron discharge plateau. In the first cycle, we used a moderate discharge rate of 200 mA. In the second cycle, we used a 50% higher discharge rate of 300 mA. Sluggish discharge characteristics are a downside of iron electrodes. In cycles 3 and 4, we investigate the phase changes for extended discharging. Our aim is to identify the iron phase of the second iron discharge plateau. Session one consists of

- Cycle 1: discharge to 0.214 Ah/g_{Fe} at a rate of 200 mA with a subsequent recharge
- Cycle 2: discharge to 0.192 Ah/g_{Fe} at a rate of 300 mA with a subsequent recharge

- Cycle 3: discharge to 0.320 Ah/g_{Fe} at rates of 200 mA first, later 100 mA with a partial subsequent recharge.
  Session 2 consists of:
- Cycle 4: discharge from 0.156 to 0.423 Ah/g_{Fe} executed with decreasing rates from 200 mA through 150 mA to finally 100 mA with a partial recharge to 0.262 Ah/g_{Fe}

The third session consists of the recharge for cycle 4 from 0.406 to 0.454 Ah/g_{Fe}. All (re)charges were programmed to slightly overcharge the electrode at a rate of 300 mA. A charge rate of 300 mA is equivalent to 46.6 mA/g_{Fe} or to a current density of 46.3 mA/cm^2 at the inner circumference of the iron electrode. The corresponding current density at the outer circumference of the counter electrode is twice as high (92.6 mA/cm^2). Table S1 of the SI provides the executed electrochemical program. Figure S3 shows the neutron diffraction pattern together with the observed electrochemical data. (Re)charging includes (1) a phase transition and (2) a hydrogen production period at the iron electrode and oxygen production at the counter electrode (Ni-wire). During discharging, the iron electrode is oxidized, while the nickel counter electrode now produces hydrogen. Equations 10–12[7] provide the overall system equations for the first discharge plateau of iron and the nickel-wire counter electrode. The half-reactions for discharging (10, E_{cell} = −0.05 V), recharging (11, E_{cell} = 1.28 V), and overcharging (12, E^0 = 1.23 V) combined give the cell reactions

$$Fe + 2H_2O \rightarrow Fe(OH)_2 + H_2 \quad (10)$$

$$2Fe(OH)_2 \rightarrow 2Fe + 2H_2O + O_2 \quad (11)$$

$$2H_2O \rightarrow 2H_2 + O_2 \quad (12)$$

Galvanostatic electrochemical experiments were executed with a Parstat MC 2000A Module. The test currents were programmed on this module. A voltmeter was used to measure the cell voltage. A second voltmeter was used to measure the voltage of the iron electrode relative to the voltage of a Hg/HgO reference electrode.

Data Processing. This study uses the GSAS-II software package for data processing.[30] For the determination of the unit cell parameters, three consecutive patterns were combined to improve counting statistics. These unit cell parameters were then used to calculate the phase fraction of the individual patterns.

It is common practice to fit phase fraction and the histogram scale factor to reach unity within one data set. Here, we follow a different approach. We fixed the histogram scale factors for all patterns. This approach allows us to track the crystalline phase fractions during an operation and to estimate how much iron-containing material is missing. For other sample parameters, the Pearl setup can be characterized as a Debye–Scherrer-type diffractometer.

Parameters for instrumental resolution were used as determined in ref 29. Initial tests indicated that the fitting quality did not improve upon fitting the instrumental parameters (U, V, and W for Gaussian and X and Y for the Lorentzian part). As these parameters remained close to the instrumental line shape, no further broadening was assumed.

Background Measurement. The individual components, sample holder, electrolyte, and counter electrode, contribute to the background in distinct ways. The quartz (SiO_2) sample holder contributes the "wavy" shape to the background signal. The pattern of the amorphous quartz has three broad peaks, at

2Θ positions 24, 44, and 88°, as shown in Figure 2. We modeled the background shape by inserting these three peaks into the background function of GSAS-II software.
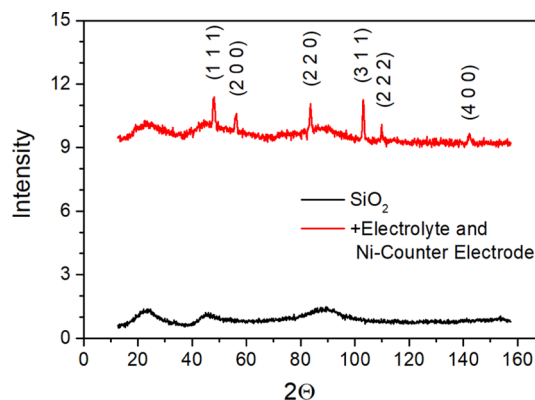

Figure 2. Intensities measured for a quartz tube (black line) and the quartz sample holder filled with 60% electrolyte (25 wt % KOH solution) together with the Ni-wire counter electrode (red line).

After final charging, the iron electrode was removed. This left the sample holder with the counter electrode and electrolyte (60% filled). The diffraction pattern of this background sample was measured. The overall intensity increases, relative to the measurement of the quartz tube alone. The shape and the wavy pattern of the quartz are still recognizable. Additional reflection peaks from the nickel counter electrode are clearly visible. This background signal is present in all measurements. All additional peaks observed in measurements with the iron electrode present would then be caused by the electrode under investigation.

Characterization of the Second Fe Discharge Phase. Iron (α-Fe) has a body-centered cubic (BCC, space group $Im\bar{3}m$, a = 2.866 Å) unit cell containing two Fe atoms. Nickel has a face-centered cubic (FCC, space group $Fm\bar{3}m$, a = 3.526 Å) unit cell containing four Ni atoms per unit cell. Iron hydroxide has a hexagonal unit cell with the space group $P\bar{3}m1$ containing one Fe atom per unit cell. Here, refinement makes use of the CIF file number COD ID 9002261 from the Crystallography Open Database (COD).[31−36] This file is based on neutron powder diffraction data collected at 300 K to study the nuclear and magnetic structures of iron hydroxide.[37]

The diffraction patterns of the most charged and the most discharged states, after subtraction of the background, are combined in Figure 3. We observed, as expected, a decrease in the diffraction intensities for iron in the discharged state. Remarkably, we found substantial and equal intensities for iron hydroxide in both states. Additional reflections, indicated with blue arrows, appear on deep discharging.

From the known iron oxides and (oxy)hydroxides (α-, β-, γ-, δ-FeOOH, α-, γ-, ε-Fe_2O_3, Fe_3O_4, FeO, and $Fe(OH)_3$), only the formation of δ-FeOOH was detectable during the second plateau discharging. So, we focused our further work on δ-FeOOH (for simulations of the diffraction patterns of iron oxides and (oxy)hydroxides, see SI, Figure S4 and Table S2). Other authors identified various other iron oxides/(oxy)-hydroxides with their measurements.[15,23−25,38−44] However, as many analytical methods require dry samples, it is entirely conceivable that some of these substances only precipitate, or even form, when drying the material. Additionally, the presence of additives affects the product that forms.
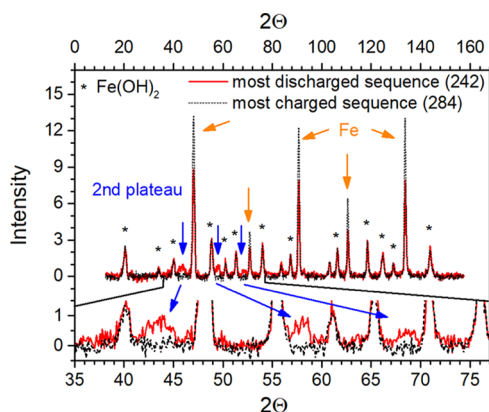
Figure 3. Top: intensities measured for the most charged pattern (284) and the most discharged pattern (242) with the background subtracted. Blue arrows indicate reflections belonging to the second Fe plateau. Orange arrows indicate varying intensities for iron. Ni is not indicated. Bottom: magnification for a 2Θ range from 35 to 7°.

δ-FeOOH is a synthetic material. The related natural compound, feroxyhyte, is also named δ'-FeOOH. They consist of a hexagonal unit cell, where the oxygen is in a similar position as in $Fe(OH)_2$. However, iron and hydrogen have additional allowed positions, doubling the number of sites in a doubled number of layers in the crystal (see Figure 4). The
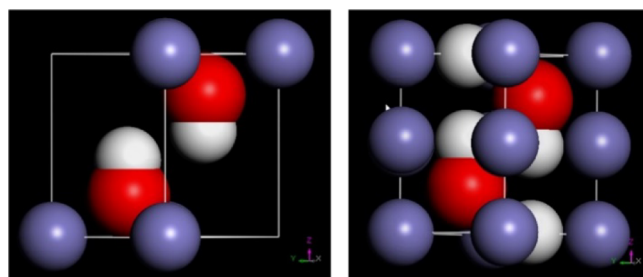

Figure 4. Left: the $Fe(OH)_2$ structure (purple: Fe, red: O, white: H). The layers between the oxygen atoms are alternatively filled with iron and hydrogen atoms. Right: δ-FeOOH structure with additional Fe and H sites that are partially occupied.

Fe^{3+} cations are distributed in an ordered manner in the synthetic compound. In the natural compound, Fe^{3+} is randomly distributed. Feroxyhyte has a slightly larger unit cell (c dimensions 0.456 nm vs 0.449 nm).[45]

To perform Rietveld refinement on neutron diffraction data, we use a symmetrical hexagonal unit ($P\bar{3}m1$) with a random distribution of the Fe ions in the octahedral sites.[46] When we investigated distorted oxygen lattices,[47] the position of the oxygen atom always converged toward symmetric spacing between the oxygen layers. When we studied displacement of the Fe ions from their octahedral site,[48] the ions also converged toward the center of the octahedron from their distorted position upon refinement. Little is known about the position of the hydrogen atom in the structure. The authors of the CIF file COD ID 1008762[47] suggest that its position is 0.120 nm above the oxygen atom in the direction of the C-axis. This leads to asymmetry in the structure, as only one layer of oxygen atoms is filled with hydrogen atoms, while the next layer is empty. The 0.120 nm O−H distance is unusually big, and the distance in a hydroxide ion is generally close to 0.096 nm (e.g., $Fe(OH)_2$: 0.094 nm). Symmetrical arrangement of

the hydrogen atoms in the suggested position inside the unit cell improved the fitting quality. Placing the hydrogen atoms closer to the oxygen atom at a distance of 0.096 nm or putting the hydrogen atoms into the tetrahedral positions worsened the fitting quality. Interestingly, distributing the hydrogen atoms symmetrically and equally between the tetrahedral sites and sites at a distance of 0.096 nm to the oxygen atom provided the same fit quality as the symmetrically rearranged hydrogen position mentioned above. Figure 5 provides the
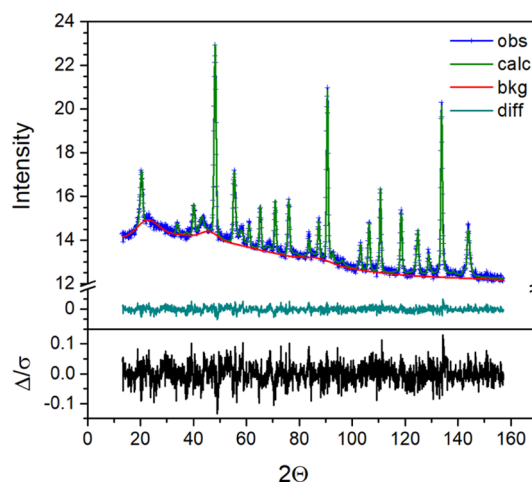

Figure 5. Top: observed intensities for the combined, most discharged pattern, 240−242 (obs), together with calculated intensities (calc), background (bkg), and difference (diff) curve. Bottom: difference curve divided by the estimated standard deviation for the data points (GSAS-II output).

final fit for the most discharged stage (averaged data from patterns 240−242), with unweighted phase residuals RF of 1.560% for iron, 1.972% for iron hydroxide, and 3.571% for δ-FeOOH. For this δ-FeOOH, the refinement yielded a characteristic crystal size of 23 nm with a microstrain of 42 000.

Note that we focused on minimizing the unweighted phase fraction with fitting due to the background. The data residuals wR result in 0.910% on 1366 observations, and χ^2 = 1.6.

Iron hydroxide and iron oxyhydroxide have the same space group, no. 164, with a different a dimension and a similar c dimension. However, the transition is more than a simple (de)protonation with additional iron and hydrogen layers occurring with partial occupation. This changes the interlayer spacing between Fe-layers and H-layers from one c-axis length to half of that and also causes fractional occupation of the sites. This has a large effect on the (001) diffraction peak at the 2Θ position 20° when comparing $Fe(OH)_2$ and FeOOH. For the $Fe(OH)_2$ pattern at this position, no large change is observed when comparing the most charged and the most discharged measurements (see Figure 4). As can be observed in SI, Figure S5 for the FeOOH phase, this peak disappears due to the shorter $c/2$ repetition of the partially occupied iron and hydrogen layers. Not only is hydrogen extracted during the transition but apparently also Fe ions and the remaining hydrogen shift in the unit cell. The oxygen atoms remain relatively unaffected. Such a relocation of transition-metal ions within the unit cell upon ions being removed from the structure is reminiscent of what happens to the Ni and Mn ion redistribution within the unit cell of ordered $LiNi_{0.5}Mn_{1.5}O_4$

upon lithium insertion into the structure; apparently, such mobility and transition-metal valence changes can induce such mobility.[49] A deconvolution of the pattern shown in Figure 5 into the individual contributions of the present phases is added to the SI, Figure S5. The derived structural parameters of all refined phases are listed in Table S3 of the SI.

Data Interpretation. The iron electrode contains 6.58 g (0.118 mol) of Fe. One Ah of charge is equivalent to 0.0373 moles of electrons. Assuming that 100% of the iron is available for a lossless two-electron process, this results in a theoretical capacity of 6.33 Ah. So, a hypothetical two-electron exchange process at a (dis)charging rate of 100 mA for an hour results in a fractional change of 0.0158 or 1.58% of the iron atoms in the electrode. Table 1 shows the theoretical fractional changes for the applied rates for one-, two-, and three-electron exchange processes.

Table 1. Expected Fractions of Affected Iron Atoms as a Function of the Inserted Charge and Fe Valence Change

electron exchange/charge rate (mAh)	$1e^-$/Fe	$2e^-$/Fe	$3e^-$/Fe
100	0.0317	0.0158	0.0106
150	0.0475	0.0237	0.0158
200	0.0633	0.0317	0.0211
300	0.095	0.0475	0.0317

Each diffraction pattern was corrected for the efficiency of the 1408 pixels of the detector. The intensity of each of the collected patterns was corrected for the variation in neutron beam intensity over the 70 h instrumental time.

Compared to hydrogen, the elements iron, oxygen, and potassium have a negligible incoherent scattering length contributing to the background. So, changes in background levels reflect the hydrogen content of the sample and electrolyte in the beam. Gas bubbles replacing liquid electrolytes are to be expected. The electrolyte has a hydrogen content of 0.108 mol H/cm^3, iron hydroxide has 0.0756 mol H/cm^3, and the same sample converted completely to Fe and the electrolyte inside the created free space has 0.079 mol H/cm^3. Consequently, the hydrogen content should hardly change during a steady first plateau transition if the gas content in the electrolyte is stable; however, it is known that gas evolution occurs readily during charging. This can alter the condensed (solid or liquid) hydrogen density in the beam. For calculations concerning the hydrogen content, see SI (Tables S4−S6).

First-Principles Calculations on δ-FeOOH. The nuclear density distribution in time of the ions in the various FeOOH structures, as well as their ground-state energies, was modeled using density functional theory (DFT) in the generalized gradient approximation (GGA), as implemented in the VASP plane-wave pseudopotential code.[50] Molecular dynamics was used at different decreasing temperatures to reach a starting structure that was subsequently minimized in a minimum energy calculation. Typically, a 2 × 2 × 2 (8-unit cells) primitive cell having 32 atoms was applied starting from several initial structures: (a) δ-FeOOH, with the appropriate randomized occupation of sites to fill the different planes for Fe and H with an average composition; and (b) a structure derived from $Fe(OH)_2$ with a composition corresponding to

Neutron diffraction pattern
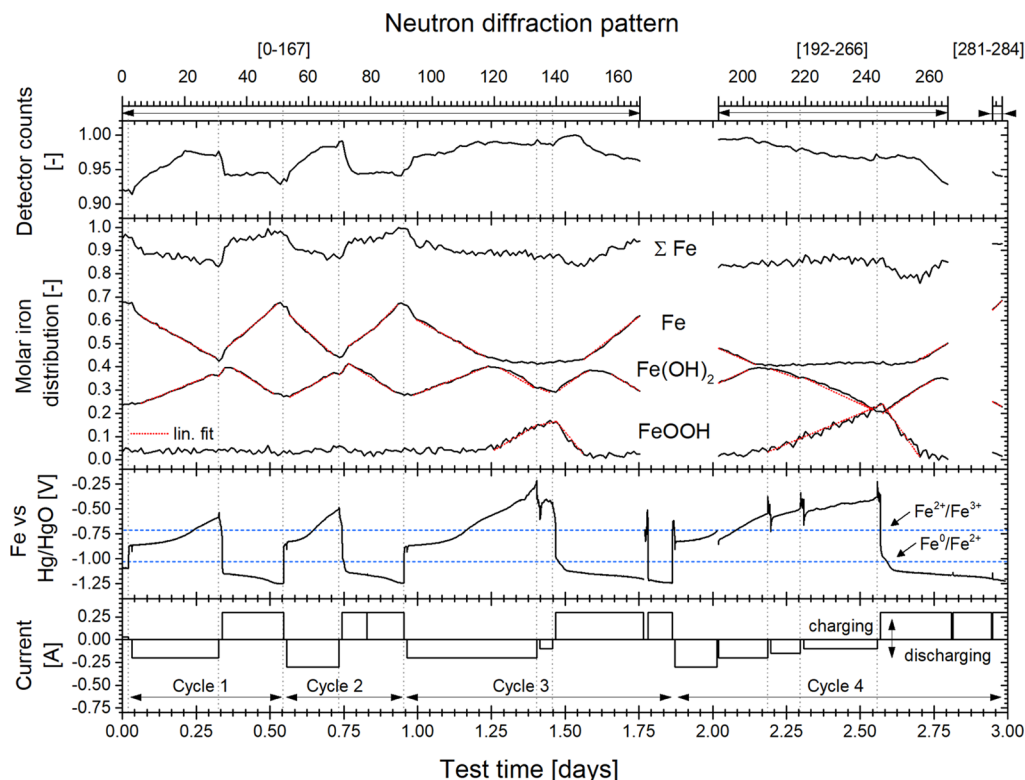
Figure 6. Detector counts, derived normalized molar iron fractions from the neutron diffraction pattern for Fe, $Fe(OH)_2$, and FeOOH with their sum, the voltage of iron electrode relative to the Hg/HgO reference electrode, and applied current. The red dotted lines indicate the linear fits depicted in SI Results Tables S6−S10. Note: the vertical gray dotted lines depict the rest periods between different experimental stages; the horizontal dashed lines depict the $Fe^{2+}(OH)_2/Fe^{3+}OOH$ and the $Fe^0/Fe^{2+}(OH)_2$ equilibrium potentials.

FeOOH (so one H removed) and lattice parameters of the δ-FeOOH.

The resulting structures are consistent with the δ-FeOOH structure, in that they have additional H planes compared to $Fe(OH)_2$, but only the structure resulting from an initial δ-FeOOH has the additional Fe plane positions. The positions of Fe and O were stable during lengthy MD simulations at 600 K and during subsequent minimization. The energies of the models are remarkably close to each other. The more random δ-FeOOH structure is only 4.8 kJ/mol lower in energy. This small difference, approximately two times k_BT, may explain a low driving force for crystallization into the δ-FeOOH form, where Fe and H form additional different planes when transforming between a H-extracted $Fe(OH_{0.5})_2$ and FeOOH, going in either direction.

It appears from these calculations that δ-FeOOH can indeed be formed in a solid-state reaction in which $Fe(OH)_2$ is dehydrogenated according to reaction 9 and where the $Fe^{3+}(OH_{0.5})_2$ subsequently partially transforms to an amorphous $Fe^{3+}OOH$ and more crystalline δ-$Fe^{3+}OOH$. The driving force to crystallize δ-FeOOH is low, which apparently makes the characteristic diffraction peak of (001) of $Fe(OH)_2$ easily disappear. Further factors leading to apparent amorphization could be the layer thickness of the materials formed upon (de-)intercalation of H; nanoscopic layer thicknesses will deform the lattice by strains in view of the different a and c parameters of the otherwise isomorphic phases.[51]

■ RESULTS AND DISCUSSION

Figure 6 depicts the parameters extracted from the neutron diffraction Rietveld refinements. The top inset shows the total detector counts as a fraction of the highest detector count we measured. The insets in the center show, in the descending order, the total amount of Fe and the calculated molar fractions for Fe, $Fe(OH)_2$, and FeOOH. The detector counts and the weight fractions are normalized to the maximum detector counts (pattern 146) and the maximum total Fe contents (pattern 89), respectively. The bottom—middle inset shows the iron electrode potential relative to the Hg/HgO reference electrode. The bottom inset depicts the cycle number and the programmed current to indicate the mode of operation (charging or discharging). A detailed analysis of the results is added to the SI, clustered into (1) start of discharging from a charged electrode, (2) steady-state discharging at the first plateau, (3) charging a discharged electrode from the first discharge plateau, and (4) the second iron discharge plateau. The following text presents and discusses the main results.

The processed results show a variation of the molar iron content between 40 and 70% for the iron metal phase and between 20 and 41% for the iron hydroxide phase. FeOOH is present from pattern 120 to 150 and from pattern 200 to 260 and reaches a molar content of 24%.

The high content of iron hydroxide is the first remarkable finding from the current work. Before testing, the cell was fully charged, followed by a floating charge for 24 h. Even so, at the start of testing, the fraction of iron hydroxide was still at 24%. So, a large fraction of the iron mass remained inactive as iron hydroxide. The literature[20,25] suggests that the passivation of iron limits the material utilization. Our data suggests that the iron electrode passivation is mostly a result of $Fe(OH)_2$ that cannot be reduced by recharging.

Figure 7 shows the derived iron content in a stacked graph with $Fe(OH)_2$, δ-FeOOH, amorphous iron phases, and

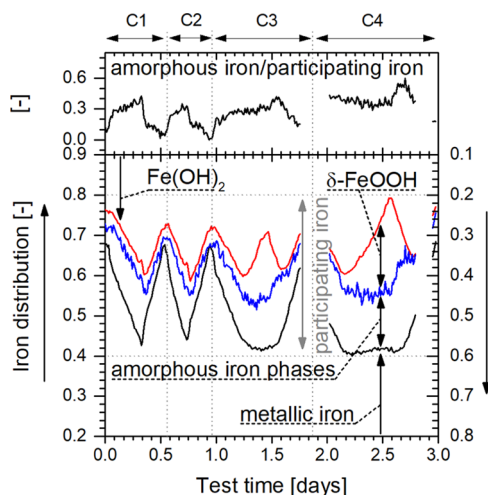**Figure 7.** Top: ratio of amorphous iron (Fe^{2+}/Fe^{3+}) phases to the participating iron. Bottom: stacked and normalized iron distribution: from top to bottom: $Fe(OH)_2$, δ-FeOOH, amorphous iron phases, and metallic iron.

metallic iron from top to bottom. We consider parts of Fe^{2+}/Fe^{3+} (oxy)hydroxides as amorphous iron-containing phases, not Fe^0. About 40% of the total iron content participates in the observed phase transitions, 20% remains inactive as iron hydroxide, and 40% remains inactive as iron. It was expected that a substantial fraction of the iron will remain inactive as iron is necessary to provide a stable physical structure and electrical conductivity. The sum of the detectable iron phases (metallic iron, $Fe(OH)_2$, and δ-FeOOH) varies upon operation and is assumed to be 100% at the observed maximum of the molar amounts of iron in the combined phase fractions. The subtraction of the iron in the combined crystalline phase fractions yields the fraction of the iron that is present in an amorphous phase. Note that it cannot be excluded that there is more amorphous material that never crystallizes. The top of Figure 7 shows the ratio of the calculated amorphous iron phase to the participating, detectable iron content. For the first plateau operation (cycles 1 and 2), the amorphous iron content shows maxima of 40% at the end of the discharge. For the second plateau operation (cycles 3 and 4), when δ-FeOOH disappears during recharging, the maxima were found around the 55% point. The high content of amorphous iron, at 22% of the sample (=0.4*0.55), is the second remarkable finding from the current work.

The increase and decrease of crystalline iron show a steep change in the transition period immediately after rest. A third of the reduction of detectable iron phases occurs in this period. This is followed by a steady rate of change for two-third of the reduction of detectable iron phases. Figure 8 shows the progress in molar amounts of iron phases during discharging of cycles 1−3 (first plateau only). Metallic iron shows steady changes in the fractional iron content that are close to the expected changes for a two-electron exchange process. The fractional changes in iron hydroxide are delayed (~35%) relative to the expected changes.

The discharge of C2 (1.5 times higher discharge rate than C1 and C3; delay of iron hydroxide formation with ~40% slightly higher) follows the pattern of C1 and C3. However, the same amount of undetectable amorphous iron phases
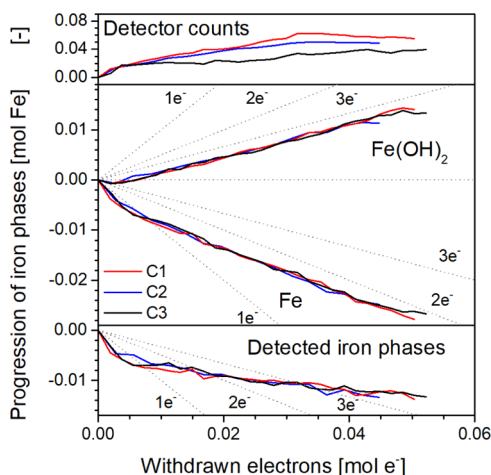
Figure 8. Progress in detector counts and molar iron amount during the discharging of cycle 1 (C1, measurements 3−30), cycle 2 (C2, measurements 53−69), and cycle 3 (C3, only the first plateau, measurements 92−120) vs inserted electrons. Top: detector counts; middle: decreasing the iron amount and increasing the iron hydroxide amount; and bottom: variation in the detectable molar iron amount. Gray dotted lines indicate the expected molar changes for a one-, two-, and three-electron process.

(0.012 mol) forms after 10% or less charge is withdrawn (at 0.045 mol e⁻ rather than at 0.05 mol e⁻).

Figure 9 shows the variation of metallic iron (Fe), iron(II) hydroxide, and detectable iron during charging. The amounts
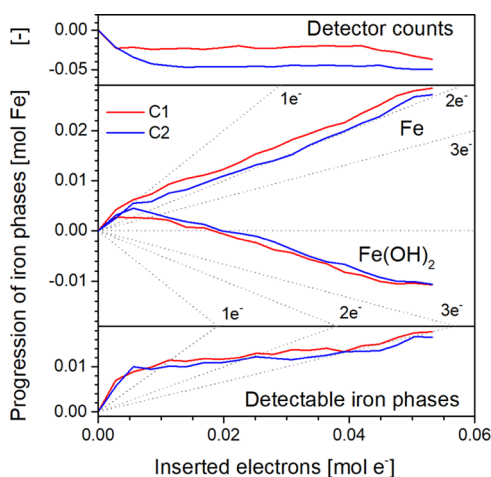

Figure 9. Detector counts and amount of iron phases during the charging of cycle 1 (C1, measurements 32−51) and cycle 2 (C2, measurements 71−90) vs inserted electrons. Top: detector counts; middle: increasing the metallic iron amount and decreasing the iron hydroxide amount; and bottom: variation in the detectable molar iron amount. Gray dotted lines indicate the expected molar changes for a one-, two-, and three-electron process.

of metallic iron and detectable iron phases increase with charging. The ratio of both at the end of charging exceeds 50%, supporting the finding that a substantial amount of iron phases must be present in the amorphous form when discharged to the first plateau. This amorphous iron phase is then reduced back to metallic iron upon charging, as is iron hydroxide. The delayed reduction of iron hydroxide alone cannot provide enough iron to cause the observed increase in metallic iron.

Interestingly, the amount of iron hydroxide first increases upon recharging before it starts decreasing. Figure 9 indicates a one-electron process for the increase in the iron hydroxide phase. We speculate that amorphous iron is present as Fe(II) and Fe(III) and that the unexpected steep increase of the iron hydroxide phase during recharging is caused by the reduction of amorphous iron(III) to crystalline iron(II) hydroxide at a higher rate than the reduction of Fe(II) hydroxide to the Fe metal. It is likely that an increased discharge rate (C2) causes a larger fraction of (amorphous) Fe(III) since the sloppy kinetics of the iron electrode cannot keep up. The increase in the iron hydroxide fraction in the transition following the discharge at higher rates is about 40% higher than in the previous transition, 4.8% compared to 3.4% (see Figure S7). The increased amorphous Fe(III) content would cause more crystalline iron hydroxide formation from the amorphous Fe(III) phase.

Both the delayed rates for iron hydroxide and the iron hydroxide formation at the start of the charging period contribute to an accumulation of iron hydroxide inside the electrode. The iron hydroxide content increased from 24 to 27% after the first recharge and to 28% after the second recharge. The initial discharge after production has a material utilization of about 0.4 Ah/g$_{Fe}$. Subsequent discharges have a utilization of about 0.15 Ah/g$_{Fe}$. This suggests that the first discharge already causes accumulation within the electrode of iron hydroxide, which cannot be fully reactivated. Discharging to the second plateau may help in reactivating iron hydroxide. The derived iron hydroxide content at the broad peaks before and after the second plateau discharge shows a reduction of 2% of the iron hydroxide content for the first shorter discharge and a reduction of 4% for the second longer discharge. In addition, the minimum iron hydroxide content at the charged state can be found at the end of our experiments, even without completed recharging.

We see a stable iron content in the different crystalline phases when iron oxyhydroxide is present in detectable amounts. When iron oxyhydroxide is no longer detectable, the phase fraction from iron metal starts increasing. From this, we conclude that no direct reduction from detected $Fe^{3+}OOH$ to Fe^0 occurs. $Fe(OH)_2$ shows broad maxima in the detected intensity before and after the transition to the second discharge plateau (see Figures 6 and 10). This smooth transition suggests a smooth solid-state reaction with Fe^{2+} going to Fe^{3+} by dehydrogenation. Moreover, it suggests that the internal charge rearrangement occurs, up to the stability limit of 10% Fe^{3+}. At higher Fe^{3+} saturation, change rates for $Fe(OH)_2$ are increasing, supporting this conclusion. The transition from the second plateau discharging to charging shows an immediate response to the current input, as can be seen from the sharp peaks for both phases. Figure 10 shows the further recharging of cycle 4.

FeOOH decreases faster than the increase seen in $Fe(OH)_2$, and the detectable crystalline iron content reaches a minimum when FeOOH has vanished, as seen in pattern 257. Then, surprisingly, both iron and iron hydroxide phases increase simultaneously. So, the reduction of amorphous Fe^{2+} to Fe^0 again takes place alongside the reduction of amorphous Fe^{3+} to $Fe^{2+}(OH)_2$. Notably, during patterns 258 and 262, we have close to perfect agreement between the measured fractional change and electrochemical charge input when assigning 66% of the charge, which contributes to the formation of Fe^0 in a two-electron process and 29% of the charge to the formation of
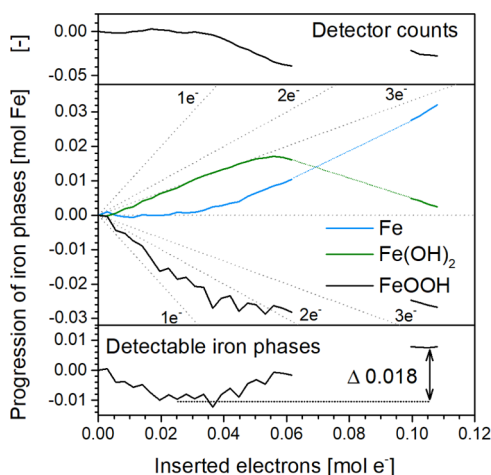
Figure 10. Progress in detector counts and amount of iron phases during recharging of cycle 4 (starting from the second discharge plateau, measurements 244−266 and 281−284) vs inserted electrons. Top: detector counts; middle: increasing the metallic iron amount, decreasing the iron oxyhydroxide amount, and first increasing and later decreasing the iron hydroxide amount; and bottom: variation in the amount of detectable iron phases. Blue and green dotted lines indicate the interpolated Fe and $Fe(OH)_2$ amounts, and gray dotted lines indicate the expected molar changes for a one-, two-, and three-electron process.

$Fe^{2+}(OH)_2$ in a one-electron process. So here, amorphous iron phases are not produced but only consumed to serve the formation of the detected crystalline phases.

Figure 11 depicts a contour plot of all recorded neutron diffraction patterns. This plot shows that reflections indicate

constant lattice parameters while the patterns vary in intensity. Changing intensities reflect the varying observable phase contents, as described earlier. In Figure 11, the incoherent background can be seen between the horizontal lines of the coherent reflections.

The background counts are linked to incoherent scattering caused by the hydrogen content inside the cell. Variations correspond with the electrolyte content as the electrolyte has the highest volumetric hydrogen density. Most significant variations are recognizable in the transition zones from charging to discharging and vice versa.

In our point of view, two mechanisms cause background variation: (1) gas production/accumulation/release and (2) material precipitation/dissolution; both result in changes of the electrolyte content.

The first mechanism can be observed, e.g., when the system is at rest. The space between the iron electrode and counter electrode is filled with gas bubbles and/or electrolyte. During an operation, the gas leaves the system via this gap. At rest, no gas is produced and the gap is refilled with the electrolyte. Because of this, the maxima in the total detector counts at rest are visible in their pattern (increased electrolyte background). When the cell is turned on again, these maxima vanish (gas replaces some electrolyte). Furthermore, hydrogen gas production also inside the electrode is indicated by the decrease in detector counts at the end of the charging step patterns 47−51 and 87−90. Note that the hydrogen evolution potential is that close to the Fe^0/Fe^{2+} equilibrium potential that the overpotential makes that hydrogen evolution can occur already from the start of charging. Here, steadily increasing (1) porosity, due to phase changes, (2) metallic iron content, and (3) cell voltage would favor hydrogen production
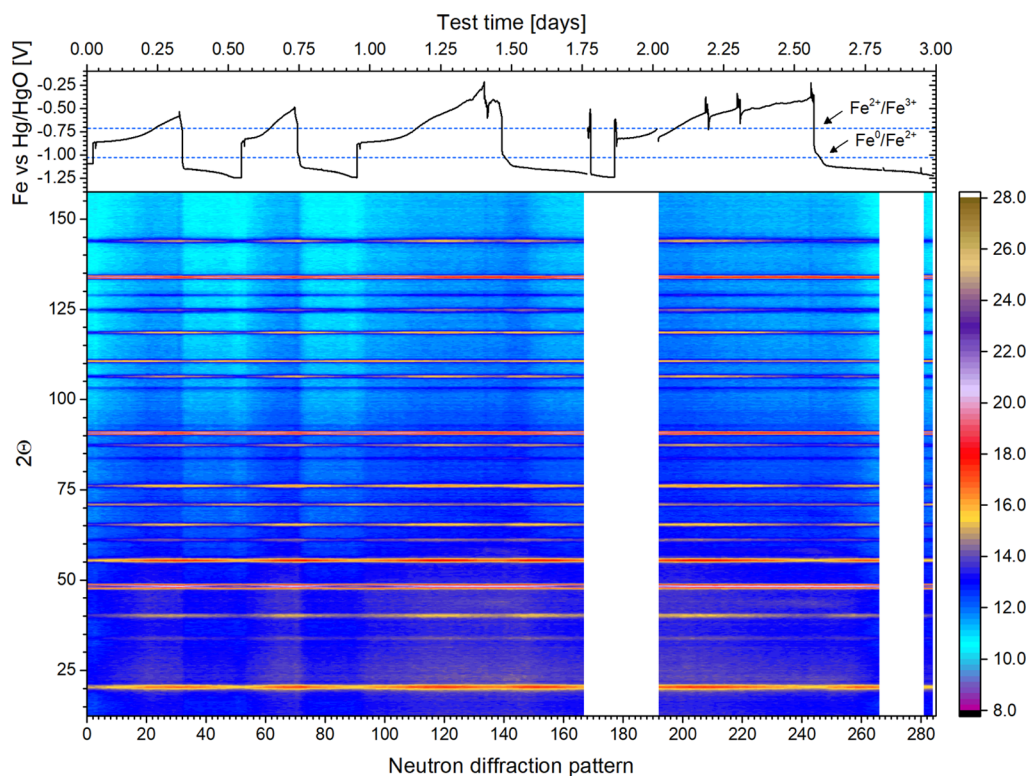

Figure 11. Contour plot of observed neutron diffraction patterns, with as a reference at the top the observed potentials of the iron electrode relative to the reference electrode (Hg/HgO) that result from the discharging, charging and waiting periods.

and accumulation. However, the stable detector counts depicted in Figure 9 indicate that in the period after the transition until the end of charging no gas accumulates within the electrode, so any produced gas can leave, keeping the content nearly constant. After prolonged charging, the voltage reaches a stable plateau, indicating that the inserted charge contributes to only hydrogen production. This is further supported by the fact that the increase in iron phase flattens out and the decrease of the iron hydroxide phase stops. Gas production is also likely to occur during the final measurement session, patterns 281−284. In these measurements, the voltage curve is already bent and close to stabilization. At this time, the detector counts are decreasing while the amount of iron is still increasing.

Gas may disappear from inside the electrode during the first two discharges (since production ceases). Here, the detector counts first increase as accumulated gas is released and then stabilize (see Figure 8). Iron and iron hydroxide show here steady gradients, suggesting no correlation between the detector counts and the phase change rates. (A discussion of a possible correlation between incoherent background affecting the screening of the samples and observed diffraction intensities is added in the SI.)

The second mechanism for changes in detector counts may be the different hydrogen contents in the solid phase precipitates. Metallic iron has no hydrogen content, and the hydrogen content of iron(II) hydroxide is lower than that of the electrolyte. At the start of the charging of C1 and C2 (see Figure 9), a substantial amount of iron and iron hydroxide forms. Also during recharging of C3 and C4, we observe a simultaneous increase of these phases but with a wider spread. The speed of change for the detector counts is correlated with the speed of phase precipitation. This correlation supports the idea that electrolyte displacement by changing precipitates occurs.

In commercial nickel−iron batteries, it is common knowledge that electrolyte levels increase during charging and decease during discharging. This characteristic can be explained by both mechanisms described, although the $Ni(OH)_2$ $NiOOH$ phase changes may play a role.

A factor of importance appears to be the gas evolution that interferes with the electrolyte content of the electrodes: the gas inside the electrode may replace the electrolyte, reducing the ionic conductivity, consistent with the observed increase in overpotentials. Moreover, the process of iron hydroxide reduction starts slowing down at the same time as the start of decrease of the detector counts that indicates gas evolution. This hydrogen can further hinder electrolyte access to any remaining iron hydroxide inside the porous structure. This would limit further $Fe(OH)_2$ dissolution necessary for iron hydroxide reduction.

Interestingly, the iron fraction increases while gas evolution takes place, so amorphous iron hydroxide still has contact with the electrolyte and can be reduced. It may be limited by poor electrolyte access as well, as the soluble intermediate Fe species requires the electrolyte, although these intermediates are reported to disappear before hydrogen evolution starts.[11,14]

Changes in the neutron screening of the sample likely affect the fractional changes in the transitions from discharging to charging. This makes both rates appear faster than they are. We observed high fractional changes of metallic iron in the transition from charging to discharging. We relate this to the start of the corrosion process of the iron electrode in the waiting period before discharging. The corrosion process is comparable to the discharge process and could provide adsorbed hydroxyl groups. With available adsorbed hydroxyl ions, fractional changes may occur at rates higher than those expected at the start of discharging.

Iron hydroxide precipitation starts with a delay after some iron is transformed into an amorphous state and iron hydroxide reduction stops when the amorphous iron has vanished. We speculate that the presence of amorphous phases is essential for a proper operation of the electrode since changes in the solid iron hydroxide phase only occur in the presence of amorphous iron phases.

■ CONCLUSIONS

In this study, we use neutron diffraction combined with Rietveld refinement to investigate the phase transitions of a sintered iron electrode in operando. This technique enables us to probe the bulk of the sample without interference.

Iron and iron(II) hydroxide are the phases forming the first discharge plateau of the iron electrode. We found that a substantial inactive amount of iron hydroxide is always present. This finding indicates that the reduction from iron hydroxide to iron needs to be improved for increased material utilization. We ascertained that crystalline iron disappears and forms as expected during an operation, while iron hydroxide reacts slowly via an intermediate amorphous phase.

The structure of δ-FeOOH fits the phase occurring at the second discharge plateau. This structure differs from that of δ-FeOOH in that it has equal spacing between the oxygen layers and symmetric distribution of the iron and hydrogen atoms. We can confirm that iron is passivated when δ-FeOOH is present and that no direct reduction from crystalline Fe^{3+} to Fe^0 occurs.

As much as 40% of the participating iron can be in an amorphous $Fe(II)/Fe(III)$-containing phase. As such, it is undetectable in the diffraction during the first plateau operation. The amount of detectable crystalline iron phases reaches an absolute minimum upon recharging when FeOOH disappears and as much as 55% of the total participating iron content is amorphous.

■ ASSOCIATED CONTENT

ⓢ Supporting Information

The Supporting Information is available free of charge at https://pubs.acs.org/doi/10.1021/acs.jpcc.1c03263.

> Extended experimental section (iron characterization, electrode production, iron oxide/hydroxide simulation, Rietveld refinement of the most discharged stage, and calculation of volumetric hydrogen content), results (starting of discharging from a charged electrode, steady gradients for the first discharge plateau, charging from the first discharge plateau, and the second iron discharge plateau, and correlation between phase precipitation and detector counts), and discussion (correlation fractional phase changes, detector counts) (PDF)

■ AUTHOR INFORMATION

Corresponding Author

Fokko M. Mulder − *Materials for Energy Conversion and Storage (MECS), Delft University of Technology, 2629 HZ Delft, Netherlands;* ⓞ orcid.org/0000-0003-0526-7081; Email: F.M.Mulder@tudlelft.nl

Authors

Bernhard M. H. Weninger − *Materials for Energy Conversion and Storage (MECS), Delft University of Technology, 2629 HZ Delft, Netherlands;* ⬤ orcid.org/0000-0002-8141-2175

Michel A. Thijs − *Neutron and Positron Methods in Materials (NPM2), Delft University of Technology, 2629 JB Delft, Netherlands*

Jeroen A. C. Nijman − *Independent researcher, 2611 GP Delft, Netherlands*

Lambert van Eijck − *Neutron and Positron Methods in Materials (NPM2), Delft University of Technology, 2629 JB Delft, Netherlands*

Complete contact information is available at:
https://pubs.acs.org/10.1021/acs.jpcc.1c03263

Notes

The authors declare the following competing financial interest(s): F.M. is co-founder of Battolyser B.V., a TU Delft spin-off company for the upscaling of integrated battery-electrolyser, or battolyser, technology.

■ REFERENCES

(1) Mulder, F. M.; Weninger, B. M. H.; Middelkoop, J.; Ooms, F. G. B.; Schreuders, H. Efficient electricity storage with a battolyser, an integrated Ni-Fe battery and electrolyser. *Energy Environ. Sci.* **2017**, *10*, 756−764.

(2) Barton, J. P.; Gammon, R. J. L.; Rahil, A. Characterisation of a nickel-iron battolyser, an integrated battery and electrolyser. *Front. Energy Res.* **2020**, *8*, No. 16505.

(3) Öjefors, L.; Carlsson, L. An iron—air vehicle battery. *J. Power Sources* **1978**, *2*, 287−296.

(4) McKerracher, R. D.; PoncedeLeon, C.; Wills, R. G. A.; Shah, A. A.; Walsh, F. C. A review of the iron—air secondary battery for energy storage. *ChemPlusChem* **2015**, *80*, 323−335.

(5) Weinrich, H.; Gehring, M.; Tempel, H.; Kungl, H.; Eichel, R.-A. Electrode thickness-dependent formation of porous iron electrodes for secondary alkaline iron-air batteries. *Electrochim. Acta* **2019**, *314*, 61−71.

(6) Yang, C.; Manohar, A. K.; Narayanan, S. A high-performance sintered iron electrode for rechargeable alkaline batteries to enable large-scale energy storage. *J. Electrochem. Soc.* **2017**, *164*, A418−A429.

(7) Weninger, B. M. H.; Mulder, F. M. Renewable hydrogen and electricity dispatch with multiple Ni−Fe electrode storage. *ACS Energy Lett.* **2019**, 567−571.

(8) Lagadec, M. F.; Grimaud, A. Water electrolysers with closed and open electrochemical systems. *Nat. Mater.* **2020**, *19*, 1140−1150.

(9) Huang, J.; Wang, Y. Efficient renewable-to-hydrogen conversion via decoupled electrochemical water splitting. *Cell Rep. Phys. Sci.* **2020**, *1*, No. 100138.

(10) Jin, Z.; Li, P.; Xiao, D. A hydrogen-evolving hybrid-electrolyte battery with electrochemical/photoelectrochemical charging from water oxidation. *ChemSusChem* **2017**, *10*, 483−488.

(11) Armstrong, R. D.; Baurhoo, I. Solution soluble species in the operation of the iron electrode in alkaline solution. *J. Electroanal. Chem.* **1972**, *34*, 41−46.

(12) Öjefors, L. Temperature dependence of iron and cadmium alkaline electrodes. *J. Electrochem. Soc.* **1976**, *123*, 1139−1144.

(13) Ravikumar, M. K.; Balasubramanian, T. S.; Shukla, A. K.; Venugopalan, S. A cyclic voltammetric study on the electrocatalysis of alkaline iron-electrode reactions. *J. Appl. Electrochem.* **1996**, *26*, 1111−1115.

(14) Armstrong, R. D.; Baurhoo, I. The dissolution of iron in concentrated alkali. *J. Electroanal. Chem. Interfacial Electrochem.* **1972**, *40*, 325−338.

(15) Ravikumar, M. K.; Rajan, A. S.; Sampath, S.; Priolkar, K. R.; Shukla, A. K. In situ crystallographic probing on ameliorating effect of sulfide additives and carbon grafting in iron electrodes. *J. Electrochem. Soc.* **2015**, *162*, A2339−A2350.

(16) Wang, H.; Liang, Y.; Gong, M.; Li, Y.; Chang, W.; Mefford, T.; Zhou, J.; Wang, J.; Regier, T.; Wei, F.; Dai, H. An ultrafast nickel—iron battery from strongly coupled inorganic nanoparticle/nano-carbon hybrid materials. *Nat. Commun.* **2012**, *3*, No. 917.

(17) Pourbaix, M. *Atlas of Electrochemical Equilibria in Aqueous Solution*; NACE, 1974; Vol. *307*.

(18) Beverskog, B.; Puigdomenech, I. Revised pourbaix diagrams for iron at 25−300 °C. *Corros. Sci.* **1996**, *38*, 2121−2135.

(19) Bernal, J.; Dasgupta, D.; Mackay, A. The oxides and hydroxides of iron and their structural inter-relationships. *Clay Miner. Bull.* **1959**, *4*, 15−30.

(20) Shukla, A. K.; Hariprakash, B. Secondary batteries − nickel systems | electrodes: iron. In *Encyclopedia of Electrochemical Power Sources*; Garche, J., Ed.; Elsevier: Amsterdam, 2009; pp 418−423.

(21) Ojefors, L. SEM studies of discharge products from alkaline iron electrodes. *J. Electrochem. Soc.* **1976**, *123*, 1691−1696.

(22) Micka, K.; Roušar, I. Theory of porous electrodes—XVIII. The iron electrode. *Electrochim. Acta* **1984**, *29*, 1411−1417.

(23) Silver, H. G.; Lekas, E. The products of the anodic oxidation of an iron electrode in alkaline solution. *J. Electrochem. Soc.* **1970**, *117*, No. 5.

(24) Geronov, Y.; Tomov, T.; Georgiev, S. Mössbauer spectroscopy investigation of the iron electrode during cycling in alkaline solution. *J. Appl. Electrochem.* **1975**, *5*, 351−358.

(25) Lee, D.-C.; Lei, D.; Yushin, G. Morphology and phase changes in iron anodes affecting their capacity and stability in rechargeable alkaline batteries. *ACS Energy Lett.* **2018**, *3*, 794−801.

(26) Falk, S. U.; Salkind, A. J. *Alkaline Storage Batteries*; John Wiley & Sons: New York, 1969.

(27) Vassie, P. R.; Tseung, A. C. C. High performance, rechargeable sintered iron electrodes—I: The effect of preparative methods and additives on the structure and performance of sintered iron electrodes. *Electrochim. Acta* **1976**, *21*, 299−302.

(28) Schimmel, H. G.; Huot, J.; Chapon, L. C.; Tichelaar, F. D.; Mulder, F. M. Hydrogen cycling of niobium and vanadium catalyzed nanostructured magnesium. *J. Am. Chem. Soc.* **2005**, *127*, 14348−14354.

(29) Van Eijck, L.; Cussen, L.; Sykora, G.; Schooneveld, E.; Rhodes, N.; Van Well, A.; Pappas, C. Design and performance of a novel neutron powder diffractometer: PEARL at TU Delft. *J. Appl. Crystallogr.* **2016**, *49*, 1398−1401.

(30) Toby, B.; Von Dreele, R. B. GSAS-II: The genesis of a modern open-source all-purpose crystallography software package. *J. Appl. Crystallogr.* **2013**, *46*, 544−549.

(31) Quirós, M.; Gražulis, S.; Girdzijauskaitė, S.; Merkys, A.; Vaitkus, A. Using SMILES strings for the description of chemical connectivity in the Crystallography Open Database. *J. Cheminf.* **2018**, *10*, No. 23.

(32) Merkys, A.; Vaitkus, A.; Butkus, J.; Okulic-Kazarinas, M.; Kairys, V.; Grazulis, S. COD::CIF::Parser: an error-correcting CIF parser for the Perl language. *J. Appl. Crystallogr.* **2016**, *49*, 292−301.

(33) Gražulis, S.; Merkys, A.; Vaitkus, A.; Okulic-Kazarinas, M. Computing stoichiometric molecular composition from crystal structures. *J. Appl. Crystallogr.* **2015**, *48*, 85−91.

(34) Gražulis, S.; Daškevič, A.; Merkys, A.; Chateigner, D.; Lutterotti, L.; Quirós, M.; Serebryanaya, N. R.; Moeck, P.; Downs, R. T.; Le Bail, A. Crystallography Open Database (COD): an open-access collection of crystal structures and platform for world-wide collaboration. *Nucleic Acids Res.* **2012**, *40*, D420−D427.

(35) Gražulis, S.; Chateigner, D.; Downs, R. T.; Yokochi, A. F. T.; Quiros, M.; Lutterotti, L.; Manakova, E.; Butkus, J.; Moeck, P.; Le Bail, A. Crystallography Open Database - an open-access collection of crystal structures. *J. Appl. Crystallogr.* **2009**, *42*, 726−729.

(36) Downs, R. T.; Hall-Wallace, M. The American Mineralogist crystal structure database. *Am. Mineral.* **2003**, *88*, 247−250.

(37) Parise, J. B.; Marshall, W. G.; Smith, R. I.; Lutz, H.; Möller, H. The nuclear and magnetic structure of "white rust"—Fe (OH0. 86D0. 14) 2. *Am. Mineral.* **2000**, *85*, 189−193.

(38) Posada, J. O. G.; Hall, P. J. Towards the development of safe and commercially viable nickel−iron batteries: improvements to Coulombic efficiency at high iron sulphide electrode formulations. *J. Appl. Electrochem.* **2016**, *46*, 451−458.

(39) Salkind, A. J.; Venuto, C. J.; Falk, S. U. The reaction at the iron alkaline electrode. *J. Electrochem. Soc.* **1964**, *111*, 493.

(40) Casellato, U.; Comisso, N.; Mengoli, G. Effect of Li ions on reduction of Fe oxides in aqueous alkaline medium. *Electrochim. Acta* **2006**, *51*, 5669−5681.

(41) Lei, D.; Lee, D.-C.; Magasinski, A.; Zhao, E.; Steingart, D.; Yushin, G. Performance enhancement and side reactions in rechargeable nickel−iron batteries with nanostructured electrodes. *ACS Appl. Mater. Interfaces* **2016**, *8*, 2088−2096.

(42) Jiang, W.; Liang, F.; Wang, J.; Su, L.; Wu, Y.; Wang, L. Enhanced electrochemical performances of FeOx−graphene nano-composites as anode materials for alkaline nickel−iron batteries. *RSC Adv.* **2014**, *4*, 15394−15399.

(43) Figueredo Rodríguez, H. F.; McKerracher, R.; de León, C. P.; Walsh, F. Improvement of negative electrodes for iron-air batteries: comparison of different iron compounds as active materials. *J. Electrochem. Soc.* **2019**, *166*, A107−A117.

(44) Manohar, A. K.; Malkhandi, S.; Yang, B.; Yang, C.; Prakash, G. K. S.; Narayanan, S. R. A high-performance rechargeable iron electrode for large-scale battery-based energy storage. *J. Electrochem. Soc.* **2012**, *159*, A1209−A1214.

(45) Cornell, R. M.; Schwertmann, U. *The Iron Oxides: Structure, Properties, Reactions, Occurrences and Uses*; John Wiley & Sons, 2003.

(46) Okamoto, S. Structure of δ-FeOOH. *J. Am. Ceram. Soc.* **1968**, *51*, 594−598.

(47) Patrat, G.; De Bergevin, F.; Pernet, M.; Joubert, J. C. Structure locale de δ-FeOOH. *Acta Crystallogr. B* **1983**, *39*, 165−170.

(48) Drits, V. A.; Sakharov, B. A.; Manceau, A. Structure of feroxyhite as determined by simulation of X-ray diffraction curves. *Clay Miner.* **1993**, *28*, 209−222.

(49) Wagemaker, M.; Ooms, F. G. B.; Kelder, E. M.; Schoonman, J.; Mulder, F. M. Extensive migration of Ni and Mn by lithiation of ordered LiMg0.1Ni0.4Mn1.5O4 spinel. *J. Am. Chem. Soc.* **2004**, *126*, 13526−13533.

(50) Kresse, G.; Furthmüller, J. Efficiency of ab-initio total energy calculations for metals and semiconductors using a plane-wave basis set. *Comput. Mater. Sci.* **1996**, *6*, 15−50.

(51) Wagemaker, M.; Singh, D. P.; Borghols, W. J. H.; Lafont, U.; Haverkate, L.; Peterson, V. K.; Mulder, F. M. Dynamic solubility limits in nanosized olivine LiFePO4. *J. Am. Chem. Soc.* **2011**, *133*, 10222−10228.